New constraints and prospects for sub-GeV dark matter scattering off electrons in xenon

Rouven Essig,[1,*] Tomer Volansky,[2,†] and Tien-Tien Yu[1,3,‡]

[1]C.N. Yang Institute for Theoretical Physics, Stony Brook University, Stony Brook, New York 11794, USA
[2]Raymond and Beverly Sackler School of Physics and Astronomy,
Tel-Aviv University, Tel-Aviv 69978, Israel
[3]Theoretical Physics Department, CERN, CH-1211 Geneva 23, Switzerland

We study in detail sub-GeV dark matter scattering off electrons in xenon, including the expected electron recoil spectra and annual modulation spectra. We derive improved constraints using low-energy XENON10 and XENON100 ionization-only data. For XENON10, in addition to including electron-recoil data corresponding to about 1–3 electrons, we include for the first time events corresponding to about 4–7 electrons. Assuming the scattering is momentum independent ($F_{DM} = 1$), this strengthens a previous cross-section bound by almost an order of magnitude for dark matter masses above 50 MeV. The available XENON100 data corresponds to events with about 4–50 electrons, and leads to a constraint that is comparable to the XENON10 bound above 50 MeV for $F_{DM} = 1$. We demonstrate that a search for an annual modulation signal in upcoming xenon experiments (XENON1T, XENONnT, LZ) could substantially improve the above bounds even in the presence of large backgrounds. We also emphasize that in simple benchmark models of sub-GeV dark matter, the dark matter-electron scattering rate can be as high as one event every ten (two) seconds in the XENON1T (XENONnT or LZ) experiments, without being in conflict with any other known experimental bounds. While there are several sources of backgrounds that can produce single- or few-electron events, a large event rate can be consistent with a dark matter signal and should not be simply written off as purely a detector curiosity. This fact motivates a detailed analysis of the ionization-data ("S2") data, taking into account the expected annual modulation spectrum of the signal rate, as well as the DM-induced electron-recoil spectra, which are another powerful discriminant between signal and background.

I. INTRODUCTION

Direct-detection experiments play a crucial role in our quest to identify the nature of dark matter (DM), and the last few years have seen intense interest and significant progress in expanding their sensitivity to particles below ∼1 GeV. The traditional direct detection technique—observing nuclear recoils from DM scattering elastically off nuclei—rapidly loses sensitivity in existing experiments for DM masses below ∼1 GeV, calling for different approaches. A demonstrated technique with significant potential for improvement is to search for DM scattering off electrons [1]. Various target materials have been investigated, including noble liquids [1,2], semiconductors [1,3–5], scintillators [6], two-dimensional targets [7], and superconductors [8,9]. These materials are also sensitive to

the absorption of ultralight DM (≪ MeV) by electrons [10–13]. For other direct-detection ideas see [1,14–20]. Direct-detection techniques and complementary probes are summarized in [21].

Currently, the most stringent direct-detection constraint on DM as low as a few MeV comes from XENON10, a two-phase xenon time projection chamber (TPC). When a DM particle scatters off an electron and ionizes a xenon atom in the liquid target, the recoiling electron can ionize other atoms if it has sufficient energy. Electric fields accelerate the ionized electrons through the liquid, across a liquid-gas interface, and propagate electrons through the xenon gas region in which interactions between the electrons and xenon atoms create a scintillation ("S2") signal that is proportional to the number of extracted electrons and detected by photomultiplier tubes. XENON10 [22] has taken data consisting of events that have an S2 signal corresponding to one or more electrons, without an observable prompt scintillation signal ("S1"). The data corresponding to events with three electrons or less ($n_e \lesssim 3$) were analyzed in [2] and shown to constrain DM as low as a few MeV.

The main factor limiting the sensitivity of XENON10 is the large number of observed S2-only events and the absence of a background model (to set a constraint, all

[*]rouven.essig@stonybrook.edu
[†]tomerv@post.tau.ac.il
[‡]tien-tien.yu@cern.ch

events are conservatively assumed to originate from DM). Plausible origins of these events include the photo-dissociation of negatively charged impurities; field emission from the cathode; and, especially, electrons that are initially created by highly ionizing background events, but then become trapped in the liquid-gas interface and spontaneously released at a later time [2,22–24]. However, more study is needed to understand and characterize these events. There are several challenges related to the background, including but not limited to multiple origins, time variation, and absence of calibration sources.

In this letter, we derive new constraints from XENON10, including events with $n_e \gtrsim 4$. The rate of observed events in this region is lower than for $n_e \lesssim 3$, leading to significantly improved constraints for DM masses $m_\chi \gtrsim 50$ MeV. We also analyze S2-only data from XENON100, containing $n_e \gtrsim 4$ [25]. We derive the expected recoil spectra for the event rate and the annual and daily modulation amplitude, and show the expected event rates and the implications for a few benchmark DM models.

Other experiments, using semiconductor targets such as germanium (Ge) and silicon (Si), currently have a higher electron-recoil energy threshold and are thus less sensitive by several orders of magnitude than XENON10/100 [5]. Dramatic improvements in sensitivity in the near future are likely with SuperCDMS [5,26], SENSEI [27], and possibly other experiments. Nevertheless, these experiments will initially have target masses of only $\mathcal{O}(1\text{ kg})$, far less than current and future xenon experiments (Table I). Understanding the S2-only events in two-phase TPCs could thus lead to dramatic improvements in cross-section sensitivity and, as we will show, probe simple and predictive benchmark models. The large exposures will also allow for an annual modulation analysis [28], which can significantly improve upon the current limit even if the background rates are high.

II. THEORETICAL RATES AND RECOIL SPECTRA

To calculate the DM-electron scattering rate in liquid xenon, we follow the procedure in [2] (see the Appendix for

TABLE I. Analyzed (XENON10, XENON100, LUX) and approximate projected (XENON1T, LZ, XENONnT) exposures and fiducial masses. We stress that future sensitivities depend on yet-unknown detector-dependent properties, such as the electron lifetime.

	Exposure [kg-yrs]	Fiducial mass [kg]
XENON10 [22]	0.041	1.2
XENON100 [25]	29.8	48.3
LUX [29]	119	145
XENON1T [30]	2,000	1,000
LZ, XENONnT [30,31]	15,000	5,600

more details). We treat the target electrons as single-particle states of an isolated atom, described by numerical RHF bound wave functions from [32,33]. The velocity-averaged differential ionization cross section for electrons in the (n, l) shell is

$$\frac{d\langle\sigma_{ion}^{nl}\rangle}{d\ln E_{er}} = \frac{\bar{\sigma}_e}{8\mu_{\chi e}^2}\int qdq|f_{ion}^{nl}(k',q)|^2|F_{DM}(q)|^2\eta(v_{min}), \quad (1)$$

where $\eta(v_{min}) = \langle\frac{1}{v}\theta(v - v_{min})\rangle$ is the inverse mean speed for a given velocity distribution as a function of the minimum velocity, v_{min}, required for scattering. We assume a standard Maxwell-Boltzmann velocity distribution with circular velocity $v_0 = 220$ km/s and a hard cutoff of $v_{esc} = 544$ km/s [34,35]. $\bar{\sigma}_e$ is the DM-free electron scattering cross section at fixed momentum transfer $q = \alpha m_e$, while the q-dependence of the matrix element is encoded in the DM form-factor $F_{DM}(q)$. $|f_{ion}^{nl}(k',q)|^2$ is the ionization form factor of an electron in the (n, l) shell with final momentum $k' = \sqrt{2m_e E_{er}}$. We calculate this form factor using the given bound wave functions and unbound wave functions that are obtained by solving the Schrödinger equation with a potential that reproduces the bound wave functions. We consider electrons in the following shells (listed with binding energies in eV): $5p^6$ (12.4), $5s^2$ (25.7), $4d^{10}$ (75.6), $4p^6$ (163.5), and $4s^2$ (213.8). The differential ionization rate is

$$\frac{dR_{ion}}{d\ln E_{er}} = N_T \frac{\rho_\chi}{m_\chi}\sum_{nl}\frac{d\langle\sigma_{ion}^{nl}v\rangle}{d\ln E_{er}}, \quad (2)$$

where N_T is the number of target atoms and $\rho_\chi = 0.4$ GeV/cm^3 is the local DM density.

We follow [2] to model the conversion from E_{er} to electron yield, n_e. The recoiling electron will ionize and excite other atoms, producing $n^{(1)} = \text{Floor}(E_{er}/W)$ additional "primary quanta," either observable electrons or (unobservable) scintillation photons. For fiducial values, we choose the probability for the initial electron to recombine with an ion to be $f_R = 0$, $W = 13.8$ eV, and the fraction of primary quanta observed as electrons to be $f_e = 0.83$. To capture the uncertainty in the fiducial values, we vary these parameters in the range $0 < f_R < 0.2$, $12.4 < W < 16$ eV, and $0.62 < f_e < 0.91$. The ranges for the parameters was chosen considering the available data and literature [36–39]. In addition to primary quanta, if DM ionizes an inner-shell electron, $n^{(2)} = \text{Floor}((E_i - E_j)/W)$ secondary quanta can be created by photons produced in the subsequent outer-to-inner-shell electron transitions with binding energies $E_{i,j}$. The number of secondary electrons produced follows a binomial distribution with $n^{(1)} + n^{(2)}$ trials and success probability f_e.

In Fig. 1, we show the recoil spectra as a function of n_e for a hypothetical xenon detector with 1000 kg-years of exposure for $F_{DM} = 1$ (top) and $F_{DM} = \alpha^2 m_e^2/q^2$ (bottom).
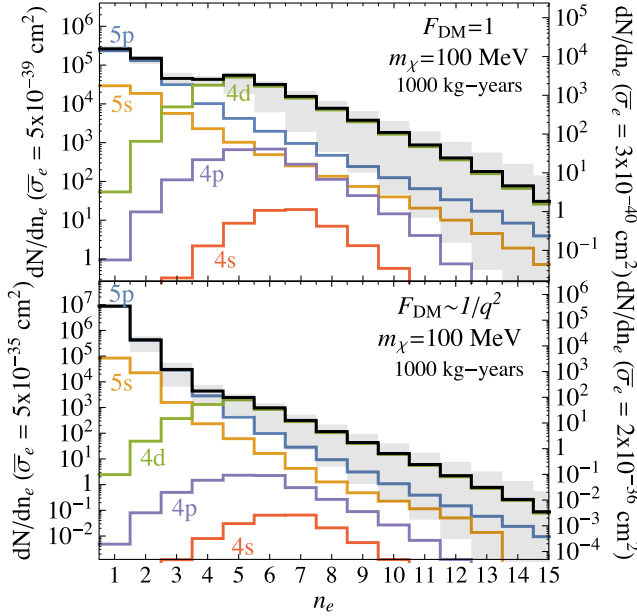
FIG. 1. Top (bottom): Spectrum of expected number of events for DM-electron scattering in xenon, for $m_\chi = 100$ MeV and 1000 kg-years for $F_{DM} = 1 (\alpha^2 m_e^2/q^2)$. For the left axes, we set $\bar{\sigma}_e$ to the maximum allowed values by current constraints for two popular benchmark models; for the right axes, the indicated $\bar{\sigma}_e$ produces the correct relic abundance. Colored lines show individual contributions from various xenon electron shells, while the gray band encompasses the spectrum when varying the secondary ionization model. See text for details.

The colored lines show individual contributions from different shells, while the black line shows their sum (for fiducial values). Gray bands show the variation away from the fiducial values discussed above.

To emphasize the importance of studying electron recoil events at current and upcoming xenon experiments, we have fixed $\bar{\sigma}_e$ to specific values that are allowed by simple and predictive benchmark models [1,5,40–46] and further below. We consider the DM (a Dirac fermion or complex scalar χ) to be charged under a broken $U(1)_D$ gauge force, mediated by a kinetically-mixed dark photon, A', with mass $m_{A'}$. The A' mediates DM-electron scattering, and $F_{DM}(q) = 1 (\alpha^2 m_e^2/q^2)$ for a heavy (ultralight) dark photon. The left axis for top (bottom) plot of Fig. 1 shows the event rate for $\bar{\sigma}_e$ fixed to the maximum value allowed by current constraints for $m_{A'} = 3m_\chi (m_{A'} \ll$ keV), while the right axis of the top (bottom) plot fixes $\bar{\sigma}_e$ so that scalar (fermion) DM obtains the correct relic abundance from thermal freeze-out (freeze-in). Clearly, a large number of DM events could be seen in upcoming detectors. These results are easily rescaled to other DM models that predict DM-electron scattering.

III. NEW XENON10 AND XENON100 BOUNDS

We now recalculate the bounds from XENON10 data [2] (15 kg-days), including for the first time events with $n_e \gtrsim 4$,

as well as from XENON100 data [25] (30 kg-years). Since the experimental observable is the number of photoelectrons (PE) produced by an event, we convert n_e to PE. An event with n_e electrons produces a gaussian distributed number of PE with mean $n_e\mu$ and width $\sqrt{n_e}\sigma$, where $\mu = 27(19.7)$ and $\sigma = 6.7(6.2)$ for XENON10 (XENON100). We multiply the signal with the trigger and acceptance efficiencies from [2,25,36], where the acceptance is taken to be a flat 0.92, and then bin both the signal and data in steps of 27 PE (20 PE), starting from 14 PE (80 PE) for XENON10 (XENON100). The first bin for the XENON100 analysis is 80–90 PE, corresponding to a width of 0.5 electron. We require that the resulting signal is less than the data at 90% C.L. in each bin. For XENON10, the 90% C.L. upper bounds on the rates (after unfolding the efficiencies) are $r_1 < 15.18$, $r_2 < 3.37$, $r_3 < 0.95$, $r_4 < 0.35$, $r_5 < 0.35$, $r_6 < 0.15 r_7 < 0.35$ counts kg^{-1} day^{-1}, corresponding to bins $b_1 = [14, 41]$, $b_2 = [41, 68] \ldots, b_7 = [176$–$203]$ PE; for XENON100, we find $r_4 < 0.17$, $r_5 < 0.24$, $r_6 < 0.17$ counts kg^{-1} day^{-1}
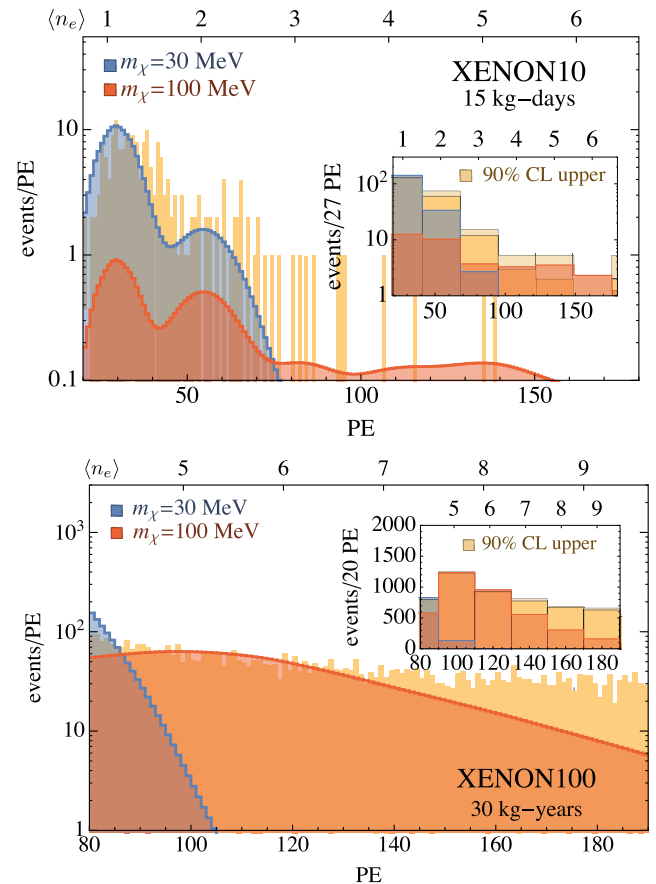

FIG. 2. Observed number of events versus photoelectrons (PE) in XENON10 (top) [22] and XENON100 (bottom) [25] (tan). DM spectra are shown for $m_\chi = 30$ MeV (blue) and 100 MeV (red) with a cross section fixed at our derived 90% C.L. limit (we assume fiducial values for the secondary ionization model). Insets show spectra in bins of 27 PE (20 PE), the mean number of PE created by one electron in XENON10 (XENON100).
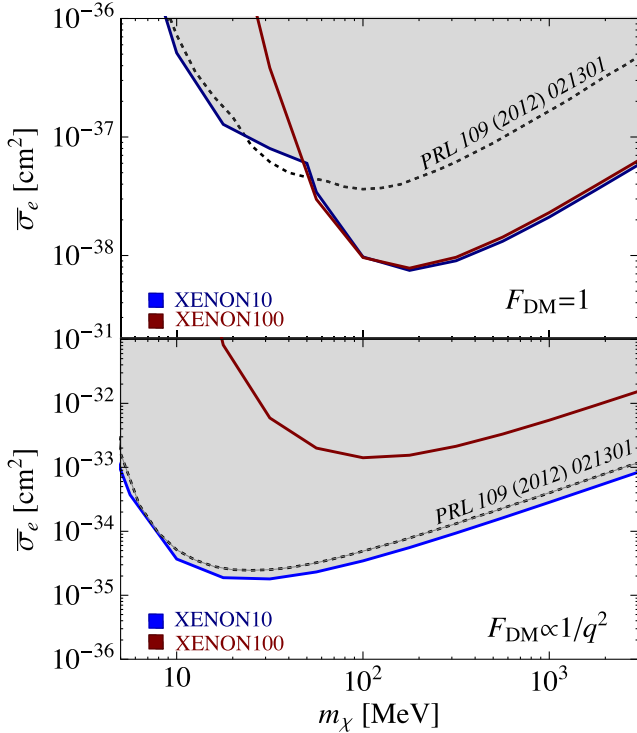
FIG. 3. 90% C.L. limit on the DM-electron scattering cross section from XENON10 data (blue) and XENON100 data (red) for $F_{DM} = 1$ (top) & $F_{DM} = \alpha^2 m_e^2/q^2$ (bottom). Dotted black lines show XENON10 bounds from [2].

corresponding to bins $b_4 = [80, 90], b_5 = [90, 110], b_6 = [110, 130]$ PE.

Figure 2 shows the two data sets in PE and two sample DM spectra. Figure 3 shows the strongest XENON10 and XENON100 limit combined across all bins, and a comparison with the XENON10 bound derived in [2]. In the Appendix, we show cross-section bounds for the individual PE bins, taking into account the systematic uncertainties from the secondary ionization model. For $F_{DM} = 1$, the inclusion of the high-PE bins in XENON10 significantly improves upon the bound from [2] for $m_\chi \gtrsim 50$ MeV (small differences at lower masses are from the limit-setting procedure). The new XENON10 and XENON100 bounds are comparable for $m_\chi \gtrsim 50$ MeV. For $F_{DM} = \alpha^2 m_e^2/q^2$, the low PE bins determine the bound, and XENON100 is therefore not competitive due to its high analysis threshold.

IV. MODULATION

A useful discriminant between signal and background is the annual modulation of the signal rate [28] due to the Sun's motion through the DM halo. Figure 4 shows f_{mod} versus n_e, where $f_{mod} = \frac{R_{max} - R_{min}}{2R_{avg}}$ is the modulation amplitude, derived by calculating the rates for the average Earth velocity and varying it by ± 15.0 km/s. The f_{mod} spectrum
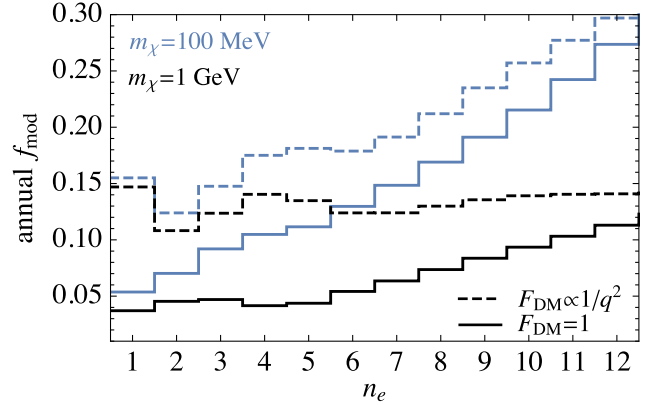

FIG. 4. Annual modulation amplitude for $F_{DM} = 1$ (solid) & $F_{DM} = \alpha^2 m_e^2/q^2$ (dashed) for $m_\chi = 100$ MeV (blue) & 1 GeV (black).

is distinctive, which should provide a helpful discriminant between signal and background. The significance of a signal S over a flat background B is then given by $sig = \frac{f_{mod}S}{\sqrt{S+B}}$.

To demonstrate the power of an annual modulation search, we imagine that a future detector with 1000 kg-years of exposure observes the *same* S2-only event rate and spectrum as observed in XENON10 data, R_{Xe10}, as given in the previous section. Requiring the signal rate to be less than the observed event rate yields the same constraints as with XENON10 data, $\bar{\sigma}_{e,Xe10}$. However, an annual modulation analysis would potentially see a signal of high statistical significance, and in the absence of one a fraction of the observed event rate must be background. Requiring the significance of the annual modulation signal to be less than sig, the expected sensitivity is

$$\bar{\sigma}_e^{mod} = \frac{sig \times \bar{\sigma}_{e,Xe10}}{f_{mod}\sqrt{R_{Xe10} \times exposure}}. \qquad (3)$$

We calculate $\bar{\sigma}_e^{mod}$ for bins of $n_e = 0.5$–$1.5, 1.5 - 2.5, \ldots$ and show with a blue line the best sensitivity across all bins in Fig. 5 for $sig = 1.65$ (90% CL) (see the Appendix for sensitivities from each bin). Similarly, a red solid line shows $\bar{\sigma}_e^{mod}$ assuming the future observed rates/spectrum correspond to the current XENON100 rate/spectrum. We overlay these lines on the DM benchmark models discussed above. However, large-scale liquid xenon detectors may not be able to detect single to few electrons in the entirety of the target mass, and so the usable fiducial volume will be smaller than the quoted values. Nevertheless, while hypothetical, this analysis emphasizes the power of an annual modulation analysis. Deriving a more realistic limit would require a dedicated study of possible time-dependent backgrounds.

Event Rates & Ann. Mod. Search, 1000 kg Xe
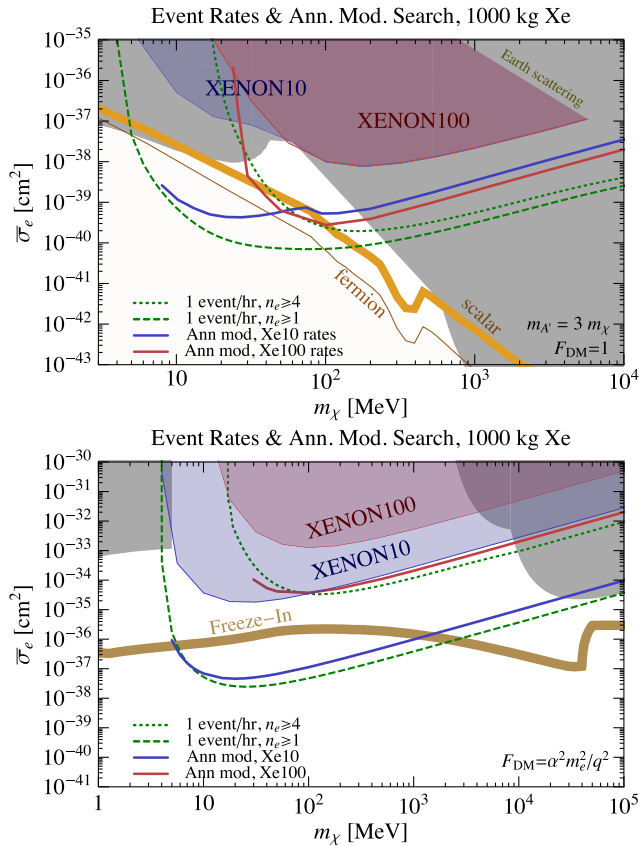

Event Rates & Ann. Mod. Search, 1000 kg Xe

FIG. 5. Sensitivity reach from an annual modulation analysis with a hypothetical 1000 kg detector and 1-year exposure, assuming the observed spectrum and data rate are the same as in XENON10 [22] (solid blue) or XENON100 [25] (solid red). DM-electron scattering event rates assuming a 1-electron (4-electron) threshold are shown in dashed (dotted) green. Blue (red) shaded regions show our XENON10 (XENON100) limits. These lines/regions are overlaid on several simple and predictive benchmark models for DM (χ) scattering off electrons via a dark photon A'. Top: ($F_{DM} = 1$) A complex scalar obtains the correct relic density from thermal freeze-out (light orange), while a fermion, which obtains its correct relic abundance from an initial asymmetry, must have $\bar{\sigma}_e$ above the dark brown line (assuming no additional annihilation channels) to avoid indirect-detection constraints [47–49]. Bottom: ($F_{DM} = \alpha^2 m_e^2/q^2$) Fermion DM coupled to an ultralight mediator A' obtains the correct relic density from freeze-in (thick brown line). Gray regions show constraints as in [5], updated on the top plot with data from MiniBooNE [50] and *BABAR* [51]. Due to earth-scattering effects [52], no XENON10/100 limit exists in the top right region.

V. LARGE EVENT RATES

To further emphasize the importance of understanding the electron recoil events in xenon TPCs, we show the expected event rates in Fig. 5 for a 1000 kg detector for two thresholds, $n_e \geq 1$ and $n_e \geq 4$. We see that the benchmark DM models predict large event rates. For example, Dirac fermion DM coupled to the A' that obtains its abundance

from an initial asymmetry could produce about one event every two seconds at LZ. This underscores the point that while there are several sources of backgrounds that can produce single- or few-electron events, a large event rate can be consistent with a DM signal and should not be simply written off as a detector curiosity.

VI. CONCLUSIONS

We derived new constraints on DM-electron scattering, improving upon the previous bound, and showed spectra for the expected number of electrons and the modulation amplitude. While there are several possible detector-specific origins of the observed XENON10/100 events, in principle almost all the observed events could originate from DM-electron scattering without coming into conflict with other existing DM constraints. This is not the case when interpreting these events as arising from few-GeV DM recoiling elastically off nuclei [22,25], which is excluded by existing results from *e.g.* LUX [53] and CDMSlite [54]. Moreover, simple and predictive DM benchmark models predict large event rates in current and future xenon TPCs. An expanded and dedicated effort by the xenon collaborations to understand the origin of their low-energy electron recoil data is thus imperative and well worth the effort.

APPENDIX

Here we provide additional details to the calculations described in the main text. We also show spectra plots for additional DM masses, as well as the XENON10/XENON100 limits and the prospects for an annual modulation analysis from each PE bin. For completeness, we also

TABLE II.   Xenon shells and energies. "Photon energy" refers to energy of deexcitation photons for outer-shell electrons deexciting to lower shells. This photon can subsequently photo-ionize, creating additional quanta. The range of additional quanta takes into account that the higher energy shell may have more than one available lower energy shell to deexcite into. For our limits, we take the minimum of this range.

Shell	$5p^6$	$5s^2$	$4d^{10}$	$4p^6$	$4s^2$
Binding energy [eV]	12.4	25.7	75.6	163.5	213.8
Photon energy [eV]	–	13.3	63.2	87.9	201.4
Additional quanta	0	0	4	6–10	3–15

show the expected daily modulation of the signal rate due to the Earth's rotation.

1. Theoretical rates

We first quote additional formulas that are required for the rate calculation (see also [2,5]). The velocity-averaged differential ionization cross section for electrons in the (n, l) shell is given in Eq. (1). The full expression for $v_{\min}$ is

$$v_{\min} = \frac{(|E^{nl}_{\text{binding}}| + E_{\text{er}})}{q} + \frac{q}{2m_\chi}, \qquad (A1)$$

where E^{nl}_{binding} is the binding energy of the shell and q is the momentum transfer from the DM to the electron. The form

factor for ionization of an electron in the (n, l) shell with final momentum $k' = \sqrt{2m_e E_{\text{er}}}$ is given by

$$|f^{nl}_{\text{ion}}(k', q)|^2$$
$$= \frac{4k'^3}{(2\pi)^3} \sum_{l'L} (2l + 1)(2l' + 1)(2L + 1)$$
$$\times \begin{bmatrix} l & l' & L \\ 0 & 0 & 0 \end{bmatrix}^2 \left| \int r^2 dr R_{k'l'}(r) R_{nl}(r) j_L(qr) \right|^2, \quad (A2)$$

where $[\cdots]$ is the Wigner 3-j symbol and j_L are the spherical Bessel functions. We solve for the radial wave-functions $R_{k'l'}(r)$ of the outgoing unbound electrons taking the radial Schrödinger equation with a central potential $Z_{\text{eff}}(r)/r$. This central potential is determined from the initial electron wavefunction by assuming that it is a bound state of the same potential. We include the shells listed in Table II.

2. Electron and photoelectron yields

We provide additional details to convert the recoiling electron's recoil energy into a specific number of electrons. The relevant quantities are

$$E_{\text{er}} = (n_\gamma + n_e)W,$$
$$n_\gamma = N_{\text{ex}} + f_R N_i,$$
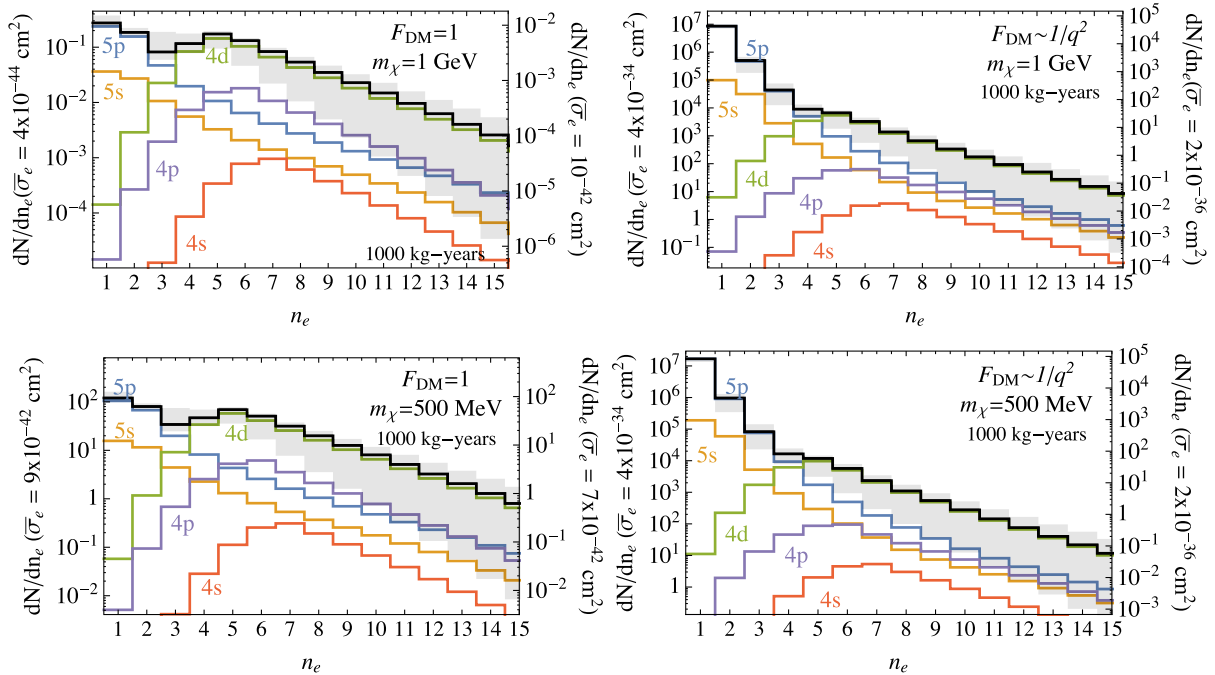$$n_e = (1 - f_R)N_i. \qquad (A3)$$

FIG. 6.   Expected number of events as a function of number of electrons observed for 1000 kg yr of xenon. The left axis sets $\bar{\sigma}_e$ to the maximum allowed value by current constraints while the right axis sets $\bar{\sigma}_e$ to the predicted value for a freeze-out (freeze-in) model for $F_{\text{DM}} = 1(\alpha^2 m_e^2/q^2)$, respectively. The different colored lines show the contributions from the various xenon shells while the gray band encodes the uncertainties associated with the secondary ionization processes.

E_{er} is the amount of deposited energy from the primary electron, which results in a number of observable electrons, n_e, unobservable scintillation photons, n_γ, and heat. W is the energy needed to produce a single quanta (photon or electron). We take $W = 13.8 \pm 0.9$ eV as the average energy [37]. E_{er} can create both a number of ions, N_i, and a number of excited atoms N_{ex}, where $N_{ex}/N_i \simeq 0.2$ at energies above a keV [37,38]. We take into account the possibility that the primary electron and secondary ions can recombine, which is described by a modified Thomas-Imel recombination model [55], and assume that the fraction of ions that can recombine, f_R, is effectively zero at low energy. This implies that $n_e = N_i$ and $n_\gamma = N_{ex}$. The fraction of initial quanta observed as electrons is given by $f_e = (1 - f_R)/(1 + N_{ex}/N_i) \simeq 0.83$ [56]. To capture the uncertainty in f_R, W, and N_{ex}/N_i, we calculate the rates and limits varying these parameters over the ranges $0 < f_R < 0.2$, $0.1 < N_{ex}/N_i < 0.3$, and $12.4 < W < 16$ eV. For our fiducial values, we set $f_e = 0.83$, $f_R = 0$, $W = 13.8$ eV.

For each primary electron with energy E_{er}, we assume that there are additional $n^{(1)} = \text{Floor}(E_{er}/W)$ quanta created. Furthermore, we assume that the photons associated with the deexcitation of the next-to-outer shells $(5s, 4d, 4p, 4s)$, which have energies $(13.3, 63.2, 87.9, 201.4)$ eV, can photoionize to create an additional $n^{(2)} = (n_{5s}, n_{4d}, n_{4p}, n_{4s}) = (0, 4, 6\text{--}10, 3\text{--}15)$ quanta, respectively (see Table II). The range in values for the $4p$ and $4s$ shells takes into consideration that there may be more than one outer-shell electron available that can deexcite down to them. For example, if the $4d$ shell deexcites to $4p$, 6 additional quanta are created, while if the $5s$ shell deexcites to $4p$, it would create 10 additional quanta. For our fiducial values, we take the lower number of quanta to be conservative. However, the choice of the number of additional quanta only affects $n_e > 6$, and even here the difference in event rate is smaller than the uncertainties due to the modeling of the secondary ionization.

The total number of electrons is given by $n_e = n'_e + n''_e$, where n'_e is the primary electron and n''_e are the secondary electrons produced. $n'_e = 0$ or 1 with probability f_R or
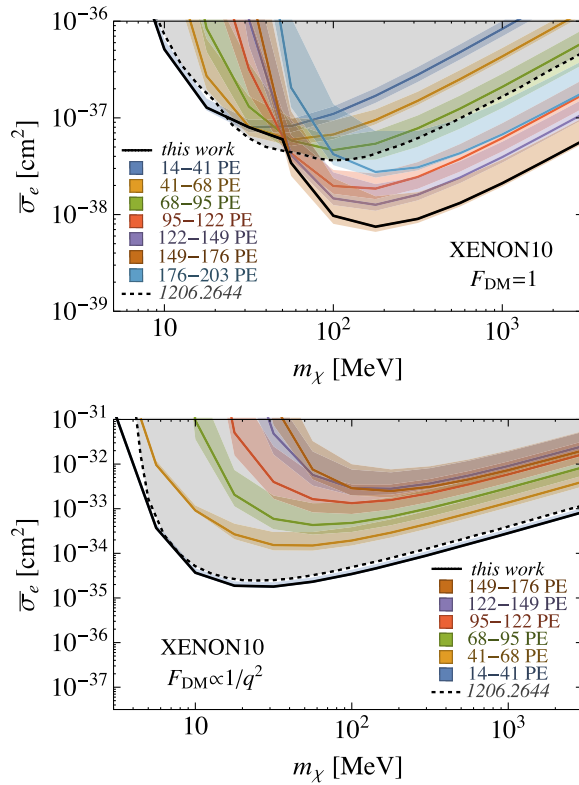

FIG. 7. New XENON10 limit (black) obtained as described in the text. The colored bands are from the uncertainty in the secondary ionization model. The shaded gray region shows the parameter space previously excluded by the 1, 2, and 3 electron XENON10 data. By including the contributions to the S2 signal from 14PE to 203PE, we see that the limits improve considerably for DM masses above ~ 50 MeV for $F_{DM} = 1$, while there is no improvement due to the momentum suppression for $F_{DM} = \alpha^2 m_e^2/q^2$.
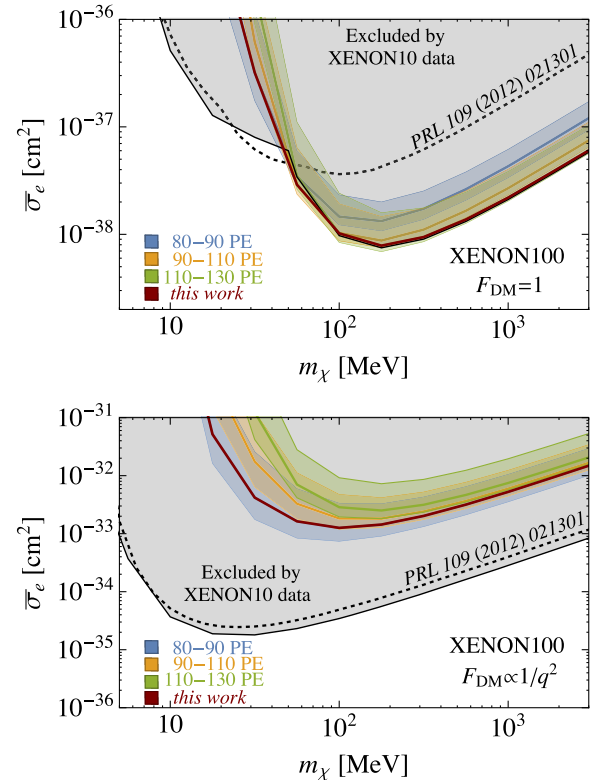
FIG. 8. New limit obtained using the XENON100 data (red). The XENON100 data starts at 80 PE electrons, so we show the individual limits for the 80–90, 90–110, and 110–130 PE bins. The colored bands are from the uncertainty in the secondary ionization model. The shaded gray region shows the parameter space excluded by our updated XENON10 analysis, while the dotted black line shows the XENON10 bound from [2].
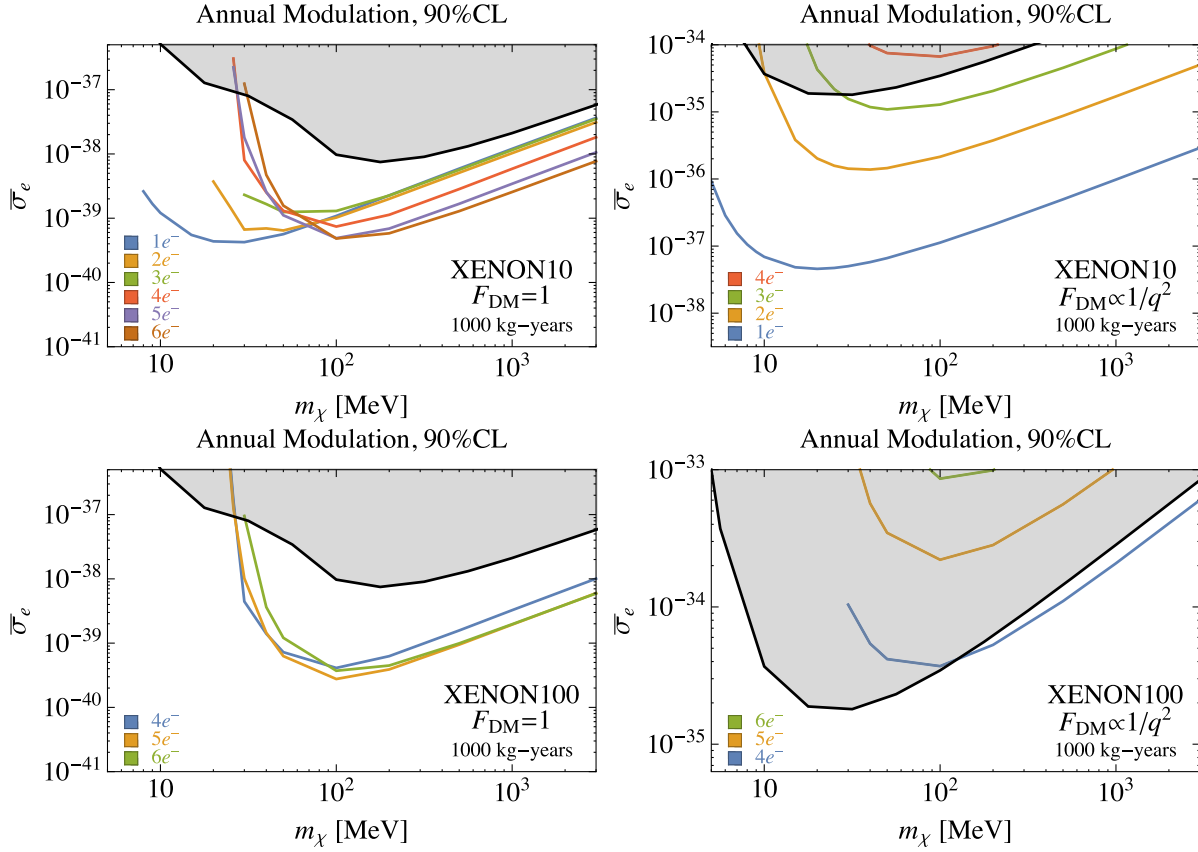
FIG. 9. Individual bin sensitivities to the 90% C.L. annual modulation reach for a 1000 kg yr xenon detector. The background rates and spectra are taken to be the XENON10 (XENON100) rates scaled up to 1000 kg yr for the top (bottom) panels (see also text and Fig. 5).

$1 - f_R$, respectively, while n_e'' follows a binomial distribution with $n^{(1)} + n^{(2)}$ trials and success probability f_e.

Given this conversion from E_{er} into n_e, we can calculate the differential rate as a function of number of electrons. In addition to the $m_\chi = 100$ MeV spectra shown in the main text, we show the spectra for $m_\chi = 500$ MeV and 1 GeV in Fig. 6.

3. XENON10 and XENON100 constraints for individual photoelectron bins

In the main text, we show the cross-section limits from the XENON10 and XENON100 data using the fiducial values above. In Figs. 7 and 8, we show the individual limits for each PE bin as well as the uncertainty bands due to the secondary ionization model.

4. Modulation

In Fig. 5, we showed how an annual modulation analysis of a hypothetical xenon detector with an exposure of 1000 kg yr could significantly improve on current constraints even if the background rates are significant. In Fig. 5, we only showed the best constraints across all individual n_e bins. In Fig. 9, we show the individual n_e bins. Furthermore, for completeness, we also show the

daily modulation amplitude due to the Earth's rotation with respect to the DM wind. The daily modulation is calculated by modifying the average Earth velocity by ± 0.23 km/s to obtain the maximum and minimum rates. We show the daily modulation fraction in Fig. 10, where we see that the daily modulation fraction is about an order of magnitude smaller than that of the annual modulation.
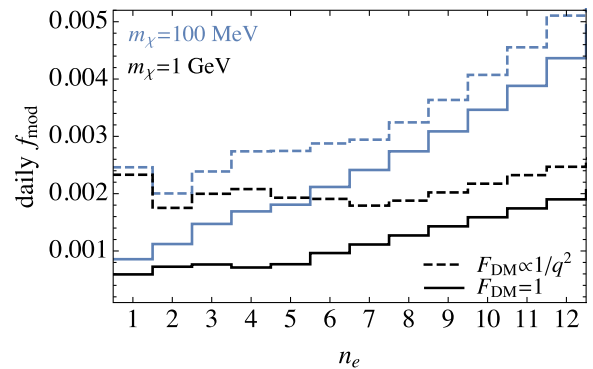

FIG. 10. Daily modulation amplitude for $F_{DM} = 1$ (solid) and $F_{DM} = \alpha^2 m_e^2/q^2$ (dashed) for $m_\chi = 100$ MeV (blue) and 1 GeV (black).

[1] R. Essig, J. Mardon, and T. Volansky, Phys. Rev. D **85,** 076007 (2012).

[2] R. Essig, A. Manalaysay, J. Mardon, P. Sorensen, and T. Volansky, Phys. Rev. Lett. **109,** 021301 (2012).

[3] P. W. Graham, D. E. Kaplan, S. Rajendran, and M. T. Walters, Phys. Dark Universe **1,** 32 (2012).

[4] S. K. Lee, M. Lisanti, S. Mishra-Sharma, and B. R. Safdi, Phys. Rev. D **92,** 083517 (2015).

[5] R. Essig, M. Fernandez-Serra, J. Mardon, A. Soto, T. Volansky, and T.-T. Yu, J. High Energy Phys. 05 (2016) 046.

[6] S. Derenzo, R. Essig, A. Massari, A. Soto, and T.-T. Yu, Phys. Rev. D **96,** 016026 (2017).

[7] Y. Hochberg, Y. Kahn, M. Lisanti, C. G. Tully, and K. M. Zurek, Phys. Lett. B **772,** 239 (2017).

[8] Y. Hochberg, M. Pyle, Y. Zhao, and K. M. Zurek, J. High Energy Phys. 08 (2016) 057.

[9] Y. Hochberg, Y. Zhao, and K. M. Zurek, Phys. Rev. Lett. **116,** 011301 (2016).

[10] H. An, M. Pospelov, and J. Pradler, Phys. Rev. Lett. **111,** 041302 (2013).

[11] H. An, M. Pospelov, J. Pradler, and A. Ritz, Phys. Lett. B **747,** 331 (2015).

[12] I. M. Bloch, R. Essig, K. Tobioka, T. Volansky, and T.-T. Yu, J. High Energy Phys. 06 (2017) 1.

[13] Y. Hochberg, T. Lin, and K. M. Zurek, Phys. Rev. D **95,** 023013 (2017).

[14] R. Essig, J. Mardon, O. Slone, and T. Volansky, Phys. Rev. D **95,** 056011 (2017).

[15] R. Budnik, O. Cheshnovsky, O. Slone, and T. Volansky (to be published).

[16] K. Schutz and K. M. Zurek, Phys. Rev. Lett. **117,** 121302 (2016).

[17] S. Knapen, T. Lin, and K. M. Zurek, Phys. Rev. D **95,** 056019 (2017).

[18] C. Kouvaris and J. Pradler, Phys. Rev. Lett. **118,** 031803 (2017).

[19] C. McCabe, arXiv:1702.04730.

[20] P. C. Bunting, G. Gratta, T. Melia, and S. Rajendran, Phys. Rev. D **95,** 095001 (2017).

[21] R. Essig, J. A. Jaros, W. Wester, P. H. Adrian, S. Andreas *et al.*, arXiv:1311.0029.

[22] J. Angle *et al.* (XENON10 Collaboration), Phys. Rev. Lett. **107,** 051301 (2011); **110,** 249901(E) (2013).

[23] E. Aprile *et al.* (XENON100 Collaboration), J. Phys. G **41,** 035201 (2014).

[24] P. Sorensen, arXiv:1702.04805.

[25] E. Aprile *et al.* (XENON Collaboration), Phys. Rev. D **94,** 092001 (2016); **95,** 059901 (2017).

[26] P. Cushman *et al.*, arXiv:1310.8327.

[27] J. Tiffenberg (SENSEI Collaboration), *SENSEI project, in Proceedings of 3rd Berkeley Workshop on the Direct Detection of Dark Matter* 2016, https://indico.physics.lbl .gov/indico/event/311/contribution/28/material/slides/1.pdf.

[28] A. K. Drukier, K. Freese, and D. N. Spergel, Phys. Rev. D **33,** 3495 (1986).

[29] D. S. Akerib *et al.* (LUX Collaboration), Phys. Rev. Lett. **118,** 021303 (2017).

[30] E. Aprile *et al.* (XENON Collaboration), J. Cosmol. Astropart. Phys. 04 (2016) 027.

[31] D. S. Akerib *et al.* (LZ Collaboration), arXiv:1509.02910.

[32] C. Bunge, J. Barrientos, and A. Bunge, At. Data Nucl. Data Tables **53,** 113 (1993).

[33] Experimental results may suggest that liquid xenon has a band structure with a gap of about 9.2 eV [34]. In this case, our calculation, which assumes an ionization energy of 12.4 eV, may underestimate slightly the true scattering rate.

[34] M. C. Smith *et al.*, Mon. Not. R. Astron. Soc. **379,** 755 (2007).

[35] W. Dehnen and J. Binney, Mon. Not. R. Astron. Soc. **298,** 387 (1998).

[36] E. Aprile *et al.* (XENON Collaboration), Astropart. Phys. **34,** 679 (2011).

[37] T. Doke, A. Hitachi, J. Kikuchi, K. Masuda, H. Okada, and E. Shibamura, Jpn. J. Appl. Phys. **41,** 1538 (2002).

[38] E. Aprile, K. L. Giboni, P. Majewski, K. Ni, and M. Yamashita, Phys. Rev. B **76,** 014115 (2007).

[39] C. Dahl, Ph.D. thesis, Princeton University, 2009.

[40] C. Boehm and P. Fayet, Nucl. Phys. **B683,** 219 (2004).

[41] N. Borodatchenkova, D. Choudhury, and M. Drees, Phys. Rev. Lett. **96,** 141802 (2006).

[42] B. Batell, M. Pospelov, and A. Ritz, Phys. Rev. D **80,** 095024 (2009).

[43] X. Chu, T. Hambye, and M. H. Tytgat, J. Cosmol. Astropart. Phys. 05 (2012) 034.

[44] T. Lin, H.-B. Yu, and K. M. Zurek, Phys. Rev. D **85,** 063503 (2012).

[45] E. Izaguirre, G. Krnjaic, P. Schuster, and N. Toro, Phys. Rev. Lett. **115,** 251301 (2015).

[46] J. Alexander *et al.*, arXiv:1608.08632.

[47] M. S. Madhavacheril, N. Sehgal, and T. R. Slatyer, Phys. Rev. D **89,** 103508 (2014).

[48] P. A. R. Ade *et al.* (Planck Collaboration), Astron. Astrophys. **594,** A13 (2016).

[49] R. Essig, E. Kuflik, S. D. McDermott, T. Volansky, and K. M. Zurek, J. High Energy Phys. 11 (2013) 193.

[50] A. A. Aguilar-Arevalo *et al.* (MiniBooNE Collaboration), Phys. Rev. Lett. **118,** 221803 (2017).

[51] J. P. Lees *et al.* (*BABAR* Collaboration), arXiv:1702.03327.

[52] T. Emken, C. Kouvaris, and I. M. Shoemaker, Phys. Rev. D **96,** 015018 (2017).

[53] D. S. Akerib *et al.* (LUX Collaboration), Phys. Rev. Lett. **116,** 161302 (2016).

[54] J. Thomas and D. A. Imel, Phys. Rev. A **36,** 614 (1987).

[55] R. Agnese *et al.* (SuperCDMS Collaboration), Phys. Rev. Lett. **116,** 071301 (2016).

[56] P. Sorensen and C. E. Dahl, Phys. Rev. D **83,** 063501 (2011).